IOP Publishing Classical and Quantum Gravity
Class. Quantum Grav. **34** (2017) 225003 (21pp) https://doi.org/10.1088/1361-6382/aa8fb5

# On tidal disruption of clouds and disk formation near boson stars

**Z Meliani[1], F Casse[2], P Grandclément[1], E Gourgoulhon[1] and F Dauvergne[1]**

[1] LUTH, Observatoire de Paris, PSL Research University, CNRS, Université Paris Diderot, Sorbonne Paris Cité, 5 place Jules Janssen, 92195 Meudon, France
[2] Astroparticule & Cosmologie (APC), CNRS/IN2P3, CEA/Irfu, Observatoire de Paris, Sorbonne Paris Cité, 10 rue Alice Domon et Léonie Duquet, F-75205 Paris Cedex 13, France

E-mail: zakaria.meliani@obspm.fr

Received 6 June 2017, revised 11 September 2017
Accepted for publication 28 September 2017
Published 25 October 2017

**Abstract**

We present two-dimensional general relativistic hydrodynamics simulations of free-falling gas clouds onto rotating boson stars (BS). Those objects consist of a complex scalar field coupled to gravity. BS are interesting as black hole (BH) mimickers. By this, one means that they are very compact objects but without any event horizon. It is then expected that the physics around BS is different than the one around BH. In this paper, we consider two BS configurations and study the trajectories and internal properties of infalling gas clouds, varying their initial positions. We follow the various disruption phases of the cloud until the formation, in some cases, of a gas torus in the inner region of the BS. We then discuss the cloud capture process by BS and the torus formation. We find that the characteristic time for torus formation increases when the initial distance between of the cloud and the BS decreases.

Keywords: boson star, tidal disruption, general relativity, numerical relativity

(Some figures may appear in colour only in the online journal)

## 1. Introduction

When a star or molecular cloud passes close to a massive compact object such as a black hole candidate (BHC), it is commonly admitted that it may be subject to tidal disruption events (TDEs). Indeed, the strong tidal field generated by the BHC is able to overcome the hydrodynamics equilibrium of the cloud/star and to tear it apart. Historically, TDEs were first proposed for theoretical considerations as a possible source for accreted matter around moderate active galactic nuclei Hills (1975). Later on, the tidal deformation of stars was investigated using

  

Newtonian gravitation (e.g. (Nolthenius and Katz 1983)) while relativistic tidal disruption effects were studied in cases of stars penetrating the inner region of the strong gravitational field of a BHC (Fishbone 1973, Carter and Luminet 1982, Luminet and Marck 1985, Marck *et al* 1996, Kobayashi *et al* 2004, Brassart and Luminet 2010). Recently, the tidal squeezing of a molecular cloud has been studied regarding the case of G2 cloud orbiting around SgrA$*$ (Schartmann *et al* 2012, Anninos *et al* 2012). TDEs were observed through soft x-ray flares for the first time in nineties by ROSAT mission (Komossa and Greiner 1999). It was followed with observations made by others *X* missions (Komossa *et al* 2004, Bloom *et al* 2011, Saxton *et al* 2015), UV-mission GALLEX (Gezari *et al* 2006) as well as optical telescopes (van Velzen *et al* 2011, Vinkó *et al* 2015). In the last decade, Swift telescope has significantly increased the number of observed TDEs while providing better coverage of their light curves. Such data provide interesting constraints to theoretical studies (Piran *et al* 2015). TDE and tidal squeezing studies also greatly benefit from numerical simulations performed either in a Newtonian (fluid and SPH scheme) or in a general relativistic framework (e.g. (Rosswog *et al* 2009, Hayasaki *et al* 2013, Shiokawa *et al* 2015)).

Studying TDE and tidal squeezing of molecular clouds is of great importance to our comprehension of BHC for many reasons as listed in Donnarumma and Rossi (2015). TDEs occurring near BHC are involved in high energy emission whose luminosity peak reaches $10^{44}$ erg s$^{-1}$ in soft x-ray band. It is noteworthy that TDEs and their resulting flares are closely related to BHC mass, spin and nature (Nikołajuk and Walter 2013). We can also mention that studying TDEs is a key to the understanding of the fueling of accretion disks occurring around some BHC (Zhao *et al* 2002). Such processes enable us to study intermediate-mass BHC (as for instance HLX-1 (Servillat *et al* 2011)) and to detect inactive BHCs in host galaxies that usually do not show any evidence of activity (Frank and Rees 1976). This is the case for the BHC located in the center of our galaxy that is currently mostly inactive despite some transient irregular events corresponding to sporadic accretion (Baganoff *et al* 2001). TDEs could then provide new perspectives to the evolution phase of AGN (radio-loud and radio-quiet) since the formation of relativistic jet during TDEs may produce transient high energy events such as Swift J1644+57 and Swift J2058.4+0516 (Burrows *et al* 2011, Bloom *et al* 2011, Cenko *et al* 2012, Metzger *et al* 2012). Finally, let us mention that TDEs may also generate gravitational waves (Kobayashi *et al* 2004, Stone *et al* 2013).

The most massive BHCs $\left(M > 10^8 M_\odot\right)$ may provoque tidal disruption from their ergosphere down to radii smaller than their Schwarzschild radius (Hills 1975). Such possibility is important when we want to infer the nature of BHC and to check if such BHC exhibits an event horizon, i.e. are truly black holes. To perform such a check, one has to investigate alternative models to the black holes. The boson star model stands as a possible alternative, being very compact and having no horizon (Bonazzola and Pacini 1966, Kaup 1968, Ruffini and Bonazzola 1969). Moreover, they are among the less exotic alternative to black holes, requiring only a massive complex scalar field to exist. Such scalar fields can date back to early stages of the Universe when stable self-gravitational pile-up soliton-type configurations occur (Schunck and Mielke 2008). The first solutions of this type were investigated by Wheeler (1955) who studied so-called *geons*, namely particle-like solutions obtained from the coupling of a classical electromagnetic field with general relativity. The field configurations found by Wheeler were, however, unstable. Later on, electromagnetic field was replaced by a complex scalar field created by spin-0 bosons in Kaup (1968) and Ruffini and Bonazzola (1969) which leads to a stable soliton solution ( e.g. Klein–Gordon geons) known as *boson star*. In such models, the boson star structure holds up against gravitational collapse thanks to the Heisenberg uncertainty principle. In the last decade, many works have been dedicated to the

nature and stability of BSs and to their possible detection (e.g. (Schunck and Mielke 2008, Liebling and Palenzuela 2012)).

In this paper we consider models for which the scalar field is a free field, thus the field is minimally-coupled to the matter. The boson star maximum mass then scales as $m_{\rm p}^2/m$ where $m_{\rm p}$ is the Planck mass and $m$ the mass of an *individual* boson described by the scalar field. Thus, the less massive the boson, the more massive is the boson star. Boson star models mainly depend on two parameters: a real period $\omega$ and a rotational quantum integer $k$ (see Grandclément *et al* (2014) for details). Let us mention that $k = 0$ corresponds to *spherically symmetric* solutions without rotation, i.e. the total angular momentum is zero. For $k > 0$ the spacetime is *axisymmetric* and has a non-zero angular momentum. Boson stars exist only if $\omega < m/\hbar$ and generate ever stronger gravitational fields as $\omega$ decreases. The structure of the gravitational field of a boson star mimics the one of a black hole at large distances. However, close to the boson star, the gravitational field differs significantly from a black hole and one can expect substantial differences in the dynamics of the inflowing gas. In particular, boson star spacetimes do not contain any horizon, so the inflowing matter may reach the inner region of the object, where the scalar field exhibits its largest amplitude, and may flow out of it. This last property of the accretion flow has to be contrasted with the black hole case where matter would disappear behind the event horizon as is shown in Meliani *et al* (2015) and Meliani *et al* (2016).

The viability of boson stars as an alternative to supermassive black holes in galactic centers and in particular for Sgr A$*$ has been investigated in great details by Torres *et al* (2000) and Vincent *et al* (2016). They showed that the available dynamical data were accurately fitted by a boson star in the very same way than a Kerr black hole. Guzmán and Rueda-Becerril (2009) also showed that a spherical boson star can indeed mimic the presence of a black hole and induce the same accretion rate. It is then one important issue to actually be able to differentiate between the two objects, which can both account for current observable constraints.

Close to the boson star, the gravitational field is very different from the one generated by a black hole so one can expect significant differences regarding the TDEs and tidal squeezing dynamics. In particular, boson stars do not contain any horizon so TDEs may happened inside the region where the maximum of the scalar field is expected. Moreover, the cloud or star could penetrate inside the boson torus. This last feature of the falling body onto the BS has to be in contrast with the black hole case where matter would disappear behind the event horizon. One can then question the fact that TDEs of stars or tidal squeezing of cloud orbiting near the BS center may reemerge from the boson star. This would be a major discrepancy between the two kinds of compact object while considering falling bodies with equivalent penetrating factor $\dfrac{r_{\rm R}}{r_{\rm P}}$ (Carter and Luminet 1982) ($r_{\rm P}$ being the pericenter radius and $r_{\rm R}$ the Roche radius).

In this paper, we present simulations constituting a first step in the study of tidal disruption of a cloud trapped by a rotating boson star. This phenomenon provides an excellent challenge for adaptive mesh refinement general relativistic hydrodynamics (AMR-GRHD) simulations, which aim at resolving the large range of both temporal and spatial scales characterizing the tidal cloud shearing. We intent to analyse the evolution of a cloud initially at rest and gravitationally bounded to the boson star. In such case, one important question remains: what would be the fraction of the cloud mass that will be trapped near the center of the BS and accordingly, how much matter can escape from the attraction of the star. Our initial setup ensures that the cloud actually travels through the BS for various BS models we consider. Another important issue related to such mass infall is the possibility to form a torus *within* the boson star, a unique feature in contrast to black holes.

Thanks to our simulations, we will infer the amount of cloud mass captured by the BS. For the sake of simplicity and numerical efficiency, we reduce the dimensionality of the simulation to two-dimensional computations, namely discarding the extension along the rotation axis of the BS. We neglect the extension of the cloud along the $z$-axis along with any flux in that direction. It implies that cloud does not experience tidal compression along the $z$-axis that may occur since the gravitational field of a BS is not necessarily symmetric with respect to the equatorial plane.. Such framework allows us to follow the evolution of the cloud within the equatorial plane but, however it prevents us from studying orbits off the equatorial plane. We then focus on determining characteristic times and scales related to the disruption of a cloud prone to the gravity of a BS. We will also investigate trajectory oscillations of the cloud induced by the BS according to its initial position. We postpone full three-dimensional simulations of TDEs around BS to a forthcoming article. This work is part of a series aiming at analysing various astrophysical scenarios related to boson stars. More informations about boson star models may be found in previous papers (Grandclément *et al* 2014, Meliani *et al* 2015, Vincent *et al* 2016, Meliani *et al* 2016).

In this paper, we focus our investigations on clouds experiencing strong tidal squeezing induced by BS. We have selected clouds initially at rest near BS as they will display trajectories crossing the BS hence experiencing the strongest possible tidal effects. It is noteworthy that the properties of other kind of trajectory related to clouds orbiting around BS are analysed in Grould *et al* (2017). We postpone the analysis of such type of cloud to a future work..

This paper is structured as follows; in section 2 we present the numerical code used to study TDEs around BS while in section 3 we present the initial setup and design of our simulations. Section 4 displays the evolution of various clouds around BS while discussing the relevant features of TDEs near BS in section 5. We finally delivers our conclusions in section 6. Throughout this paper we will use units where the speed of light $c = 1$, the gravitational constant $G = 1$, and gas mass is normalized to the central compact object mass $M$. The distances are normalized to the Schwarzschild radius defined from the (equivalent) mass of the central object. Concerning the density and the pressure, the normalisation is given by the density number $n_0$, such $[\rho] = n_0 M$ and the pressure norme is $[p] = n_0 M c^2$. Roman indices refer to spatial dimensions, taking only values $\{1, 2, 3\}$. We assume a signature $(-, +, +, +)$ for the spacetime metric.

## 2. Numerical method

The simulations presented in our paper are performed using the GR-MPI-AMRVAC code (Meliani *et al* 2016), which solves the differential equations for mass, momentum and energy conservations, namely

$$\begin{aligned}
&\frac{\partial \sqrt{\gamma} D}{\partial t} + \partial_{\mathrm{i}} \left( \alpha \sqrt{\gamma} D \hat{v^{\mathrm{i}}} \right) &&= 0, \\
&\frac{\partial \sqrt{\gamma} S_{\mathrm{j}}}{\partial t} + \partial_{\mathrm{i}} \left( \alpha \sqrt{\gamma} \left( S_{\mathrm{j}} \hat{v^{\mathrm{i}}} + P \delta^{\mathrm{i}}_{\mathrm{j}} \right) \right) &&= \sqrt{\gamma} \left( \frac{1}{2} \alpha \left( S^{\mathrm{i}} v^{\mathrm{k}} + P \gamma^{\mathrm{i}\,\mathrm{k}} \right) \partial_{\mathrm{j}} \gamma_{\mathrm{i}\,\mathrm{k}} + S_{\mathrm{i}} \partial_{\mathrm{j}} \beta^{\mathrm{i}} - (\tau + D) \partial_{\mathrm{j}} \alpha \right), \\
&\frac{\partial \sqrt{\gamma} \tau}{\partial t} + \partial_{\mathrm{i}} \left( \alpha \sqrt{\gamma} \left( \tau \hat{v^{\mathrm{i}}} + P v^{\mathrm{i}} \right) \right) &&= \sqrt{\gamma} \left( \frac{1}{2} \left( S^{\mathrm{i}} v^{\mathrm{k}} + P \gamma^{\mathrm{i}\,\mathrm{k}} \right) \beta^{\mathrm{j}} \partial_{\mathrm{j}} \gamma_{\mathrm{i}\,\mathrm{k}} + \left( S_{\mathrm{i}} v^{\mathrm{j}} + P \delta^{\mathrm{j}}_{\mathrm{i}} \right) \partial_{\mathrm{j}} \beta^{\mathrm{i}} - S^{\mathrm{j}} \partial_{\mathrm{j}} \alpha \right),
\end{aligned} \tag{1}$$

with $v^{\mathrm{i}} = u^{\mathrm{i}}/W + \beta^{\mathrm{i}}/\alpha$ being the fluid three-velocity with respect to the zero-angular momentum observer (ZAMO), while $W = \alpha\, u^{\mathrm{t}} = 1/\sqrt{1 - v_{\mathrm{i}}\, v^{\mathrm{i}}}$ stands for the related Lorentz factor. We also introduce the transport velocity $\hat{v^{\mathrm{i}}} = u^{\mathrm{i}}/\alpha u^{\mathrm{t}} = v^{\mathrm{i}} - \beta^{\mathrm{i}}/\alpha$, where $u^{\mu} = \left(u^0, u^{\mathrm{i}}\right)$ is the

four-vector velocity. The thermal pressure of the gas is denoted by $P$. The conservative variables of GR-HD equations are: the density as measured by the ZAMO, $D = W\rho$ with $\rho$ being the comoving density, the momentum $S_{\rm j} = W^2\rho h\, v_{\rm j}$ while $\tau + D = W^2\rho h - P$ represents the total energy density of the gas. The specific enthalpy reads $h = 1 + \epsilon + \frac{P}{\rho}$ where $\epsilon$ is the specific internal energy. Regarding the spacetime, the line element is given by

$$\mathrm{d}s^2 = -\alpha^2\mathrm{d}t^2 + \gamma_{\rm i\,j}\left(\mathrm{d}x^{\rm i} + \beta^{\rm i}\,\mathrm{d}t\right)\left(\mathrm{d}x^{\rm j} + \beta^{\rm j}\,\mathrm{d}t\right), \tag{2}$$

where $\gamma$ is the spatial metric determinant, $\alpha$ the lapse function, $\beta^i$ the shift vector and $\gamma_{\rm ij}$ the spatial metric tensor.

Regarding the simulations performed in this paper, we use the cartesian quasi-isotropic coordinates. The boson star metric elements are computed numerically thanks to a numerical code built on the KADATH library (Grandclément *et al* 2014). The KADATH code provides metric elements as well as their derivatives every time a new grid is generated by adaptive-mesh-refinement techniques within the GR-MPI-AMRVAC code (Meliani *et al* 2016). Let us mention that the provided metrics are expressed in spherical quasi-isotropic coordinates so that we convert them inside GR-MPI-AMRVAC to cartesian quasi-isotropic coordinates.

## 3. Initial setup and boson stars models

As already mentioned in the introduction, we deliberately neglect the initial thickness of the cloud orthogonal to the equatorial plane while assuming that the gas is unmagnetized. In our scenario, we consider a cold cloud free falling onto a rotating boson star. Since the cloud is set near the compact object, the gravitational force of the latter is much larger than the self-gravity of the cloud so that we can safely neglect it. During the compression phases, the cloud undergoes an important elongation which limits the amplitude of its self-gravity.

We investigate three different cases of falling cloud with varying initial positions of the cloud while considering two models of BS: ($k = 1, \omega = 0.8\ m/\hbar$) and ($k = 4, \omega = 0.8\ m/\hbar$). The first BS model is depicted in figure 8 of Grandclément *et al* (2014). We set up the gas sphere at a distance $r_{\rm start} = 23\,M$ (in case (A) and (C)) and $r_{\rm start} = 3\,M$ in case (B). In all cases the sphere has a Gaussian density distribution with a standard deviation $\boldsymbol{R}_{\rm sphere}$ The density at the cloud center is $\rho = 10^{-1} n_0\, M$ and the pressure is set to a low value, namely $p = 10^{-7} n_0\, M$. The external medium has low density $\rho_{\rm ext} = 10^{-6} n_0\, M$ compared to the cloud and the same thermal pressure than the sphere. Thereby the cloud is initially in pressure equilibrium with the external medium. The initial values for density and thermal pressure are chosen so that the self-gravity of the cloud remains negligible compared to the gravity of the BS while ensuring that the external medium has no influence on the cloud structure. We denote by $n_0$ the normalization parameter for the density. This parameter leads to the physical value of the density of the cloud provided an equivalent mass of the BS has been chosen. In our simulations, $n_0$ has to be set so that the mass of the cloud remains negligible compared to the equivalent mass of the BS. At the initial state, all clouds are montionless and do not have any angular momentum. The parameters of the three cases we consider in this paper are listed in table 1.

The simulation is performed using a Cartesian grid on domain $[-30\,M, 25\,M] \times [-30.\,M, 25\,M]$ for simulations A and C while we set the domain to $[-6\,M, 6\,M] \times [-6\,M, 6\,M]$ for simulation B. We use a base resolution of $120 \times 120$ allowing 8 (simulations A and C) and 5 (simulation B) additional levels of refinement, each doubling the local resolution reaching an effective resolution of $15\,360 \times 15\,360$ cells in simulations A and C while we reach a resolution of $1920 \times 1920$ cells for simulation B. This gives us an effective spatial resolution of $3.485 \times 10^{-3}\,M$ for cases A and C and $3.186 \times 10^{-3}\,M$ for case B. All the simulations

**Table 1.** Parameters of the various simulations: the boson star rotational quantum integer $k$ and real period $\omega$, the density and pressure of the external medium, the initial density, radius and initial position of the cloud.

| | Boson star | | External medium | | | Cloud | |
|---|---|---|---|---|---|---|---|
| Case | $k$ | $\omega\ (m/\hbar)$ | $\rho_{\rm ext}(n_0\,M)$ | $p_{\rm ext}(n_0\,M\,c^2)$ | $\rho_{0,\ \rm cloud}(n_0\,M)$ | $R_{\rm sphere}$(M) | Initial position (M) |
| A | 1 | 0.8 | $10^{-6}$ | $10^{-7}$ | $10^{-2}$ | 0.70 | 23 |
| B | 1 | 0.8 | $10^{-6}$ | $10^{-7}$ | $10^{-2}$ | 0.01 | 3 |
| C | 4 | 0.8 | $10^{-6}$ | $10^{-7}$ | $10^{-2}$ | 0.70 | 23 |

**Table 2.** Main cloud evolution phases for the three cases. In all cases, the cloud undergoes a strong tidal compression shocks.

| Case | Tidal stretching | Periodic tidal compression shock | Disc formation |
|---|---|---|---|
| A | Strong | No | Yes |
| B | Weak | Yes | No |
| C | Strong | Yes | Yes |

employ a HLL scheme (Harten *et al* 1983) coupled to a Koren limiter (Koren and van der Maarel 1993), and use the second order Rung–Kutta time integration scheme. The boundary conditions in all directions are set to prevent any in-falling gas to enter the simulation domain.

## 4. Free-falling clouds onto boson stars

In this section, we will describe the cloud evolution phases for all cases (A)–(C). And the main evolution phases for the three cases are given in table 2.

### *4.1. Remote cloud around a typical boson star—Case A*

In this first simulation, the molecular cloud is initially set at a distance $r_{\rm start} = 23\,M$ from the center of the boson star whose parameters are $k = 1$ and $\omega = 0.8\ m/\hbar$.

*4.1.1. Initial falling of the cloud.* During the first phase of the free-fall, the cloud basically follows the local geodesic (figure 1) without experiencing any deformation. The cloud then moves along the radial direction until it approaches the BS ($r_1 < 3\,M$) where it experiences a toroidal acceleration induced by the frame dragging effect in the direction of the BS rotation, namely the counter-clockwise direction.

The tidal stretching of the cloud is initiated as soon as the cloud begin to fall toward the center of the BS. Beyond $r > 15\,M$, the cloud experiences the same gravitational force as if the central object was a BH. Indeed, at larger distance, metric elements of BS and BH are very similar (Meliani *et al* 2016). However, within $r < 15\,M$ the strength of the gravity of the BS increases, but since the corresponding lapse function exhibits a smoother radial variation compared to the BH case, the associated tidal gravitational force does have a smaller amplitude than near a BH.

The initial position of the cloud being $r_{\rm start} = 23\,M$, the cloud experiences mainly a radial acceleration while undergoing a small deviation in the toroidal direction. As the cloud moves closer to the BS torus, its radial speed reaches a value of $v^{\rm r} \sim 0.54\,c$ smaller (but close) to

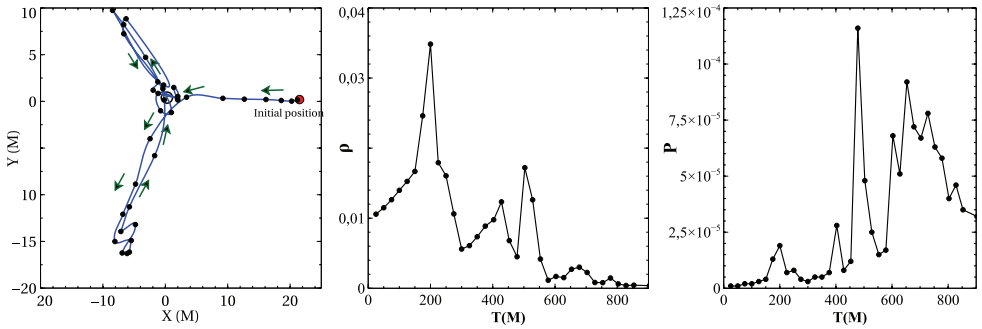


**Figure 1.** Case (A). Left: the free-falling orbit of the cloud in the vicinity of a boson torus with $k = 1$ and $\omega = 0.8\ m/\hbar$; the small black circle around the center marks the maximum of the scalar field, where the BS rotates in counter-clockwise direction. Center: the maximum density $\rho$ (in $n_0 M$ units) found in the cloud as a function of time. Right: the maximum pressure $p$(in units of $n_0 M c^2$) temporal evolution. The maximum density and pressure occur near the cloud head along its propagation axis.

the escape velocity from the center of BS torus ($0.73c$). During this first acceleration phase, the shear of the flow at the cloud edges leads to the formation at a turbulent tail of the cloud (figures 2 and 4) similar to the results obtained in Schartmann *et al* (2012). The high resolution of our simulation enables us to capture the development of Kelvin–Helmholtz instabilities enhanced by Rayleigh–Taylor instabilities. These instabilities result from the strong tidal oblique compression waves that cross the cloud during the free fall phase. These waves increase the density and the pressure of the cloud and induces acceleration toward cloud propagation axis and toward the external medium. The deviation of the cloud trajectory from the local geodesic remains small during this phase (figure 1, left). As the cloud moves toward the center of the BS, the tidal force across the cloud increases and the shape of the cloud changes continuously. The radial stretching and transverse compression during this phase leads to a modified shape of the cloud, switching from its initial ball-shape to a drop-shape (Schartmann *et al* 2012). The elongated shape has an extension of $L = 4M$ along the propagation direction and a low transverse width of $0.35\,M$. During this free-falling phase there are no mass loss from the cloud.

Successive transverse strong compressions of the cloud occur during the falling phase leading to the cloud being squeezed perpendicularly to the propagation direction. This compression appears through the growth of the thermal pressure in the cloud (figure 1, right) as in Luminet and Marck (1985). Since the cloud is free-falling onto a BS, it is also subject to a tidal stretching occurring along the propagation direction. This stretching effect counterbalances the increase of thermal pressure induced by the transverse compressions. The resulting gas distribution is then more elongated along the propagation direction (figure 4) leading to an enhanced transverse squeezing (Brassart and Luminet 2010). During this phase the sound speed inside the cloud reaches a peak value of $c_s = 0.1\,c$.

Looking more closely at the shock wave pattern in the cloud, we can see that both compressional and shock waves are oblique to the cloud propagation axis. Each time one of these waves (faster at the head of the cloud than at the tail) reaches the main propagation axis it bounces back to the edge of the cloud. The returning wave then collides with the successive forming compressional wave/shocks at the edge of the cloud. As time goes by, the strength of compressional waves increases while the cloud approaches the BS, and after time $100\,M$, they turn into shock waves. Accordingly, Mach number increases from $\mathcal{M} = 0.1$ to $\mathcal{M} = 1.1$

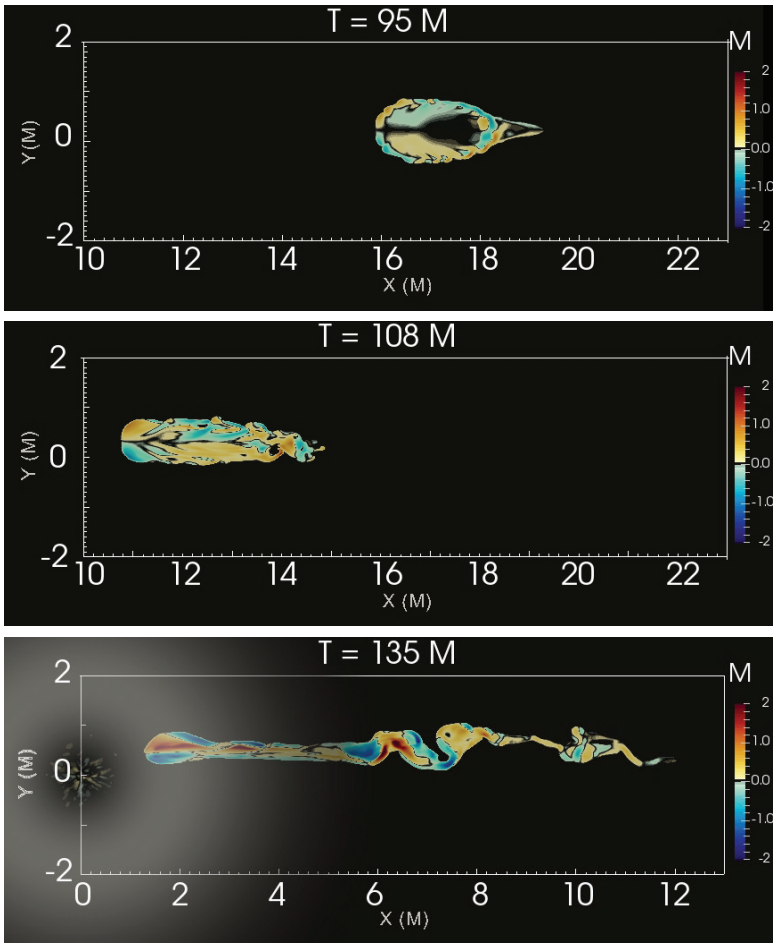


**Figure 2.** Colormap of the Mach number of the gas contained in the cloud measured in the comoving frame. The three plots stand for three snapshots of the simulation during the first free-fall phase of the cloud in the vicinity of a BS with $k = 1$ and $\omega = 0.8m/\hbar$ (Case A). Let us mention that the BS center is located at the origin.

(figure 2). During the free-falling phase, namely $T \leqslant 100\,M$ where the cloud is located beyond $r \sim 15\,M$, the compression is weak and the thermal pressure is slowly increasing (figure 1, right). Afterward the thermal pressure of the cloud rises more rapidly after time $100\,M$. We also note that beyond that time, the orientation of the shock waves orientation becomes parallel to the propagation axis, especially at short distance from the center. Such waves reach a maximum Mach number of the order of $\mathcal{M} \sim 2$ (figure 2, time $T = 135\,M$). It is noteworthy that the strongest shocks are propagating in the opposite direction to the BS rotation. Such clockwise orientation of the strongest waves is induced by the frame-dragging occurring in the direction of BS rotation (which is anticlockwise). In the end a larger tidal squeezing rise in the upper part of the cloud (figure 2).

*4.1.2. Crossing through the BS.* At short distance from the center $r < 3\,M$, the frame dragging effect becomes important as can be seen on the right panel of figure 3. The cloud is then drifted toroidally to reach a speed of $v^{\varphi} \sim 0.1\,c$ in the same direction as the BS rotation

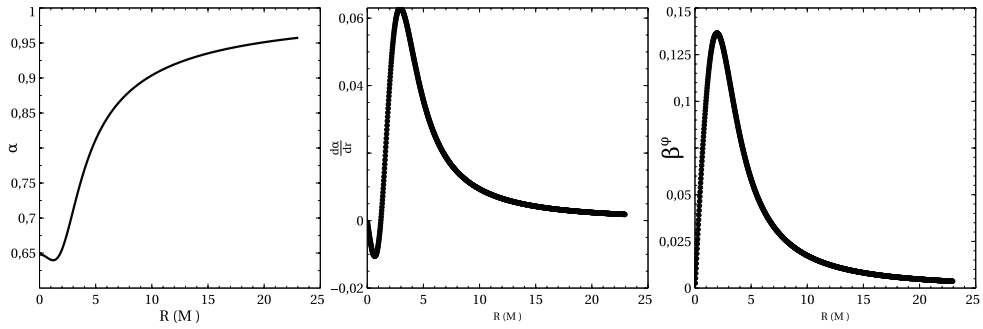


**Figure 3.** Radial profile of various spacetime quantities for the BS model considered in simulations $(A, B)$. Left: lapse function $\alpha$. Center: radial derivative of the lapse function $\frac{d\alpha}{dr}(M^{-1})$. Right: the toroidal components of the shift vector $\beta_\varphi$(in units of $c$) characterizing the frame-dragging occurring neat the BS center.

(figure 4). The toroidal deviation is first triggered at the head of the cloud and then at the cloud tail, inducing an arc structure on the cloud (figure 4). At time $T = 135\,M$ the cloud crosses the region where the scalar field reaches its maximum amplitude leading to another deviation between this point and the geometrical center of the BS where the scalar field vanishes. At this point, the angle between the propagation direction and the $x$-axis is of order of $\varphi = 26°$. During this phase, the radial speed remains constant. However, the cloud gets more and more gravitationally squeezed until it collapses into a spaghetti-like shape as in the simulation done in the non-relativistic case (Schartmann *et al* 2012). When the cloud crosses the geometrical center, it has deviated 120° from its initial propagation direction. At this stage, the cloud is deviated in the same direction of BS rotation and goes through a large deviation, thus it looks like the cloud is scattered in opposite to the BS rotation direction. At the center, the cloud thermal pressure reaches its maximum value $p \sim 2.5 \times 10^{-5}\,(n_0\,M\,c^2)$ (figure 1) and density attains $\rho \sim 0.036\,(n_0\,M)$ . The radial motion of the cloud is then supersonic as the sound speed reaches $c_s = 0.01c$.

*4.1.3. Emerging from the BS.* The head of the cloud having reached a large velocity of the order of $v^r = 0.5c$, it escapes from the interior of the BS. While escaping, the head of the cloud has mainly a radial trajectory with a low deviation in the toroidal direction (toroidal speed of $v^\phi = 0.01c$). Let us mention that the radial component of the velocity is larger than the frame dragging speed, namely $\beta^\varphi = 7.224 \times 10^{-2}\,c$ (figure 3, right). Once the cloud has emerged from the BS, its head starts to decelerate because of the gravitational force of the BS. The radial motion eventually stops at a distance of $r = 40\,M$ from the center of the BS (figures 1 and 4). Tidal disruption being also at work during the outgoing phase, the cloud stretching increases as the tail of the cloud remains at the BS center during all this phase. While staying near the center of the BS, the tail of the cloud gets twisted by the Lense–Thirring effect as expected since its radial velocity component is smaller than the frame dragging speed. Such Lense–Thirring effect then produces an extended arc shape in the tail of the could (figure 4, top).

It is noteworthy that while the head of the cloud propagates away from the center, the transverse gravitational force rapidly decreases, leading to a thermal expansion of the cloud in the toroidal direction. The sound speed of the head of the cloud being of the order of the drag frame speed, the cloud expansion mainly occurs in the direction of the boson star rotation. On the other hand the expansion in the opposite direction gets limited by the Lense–Thirring

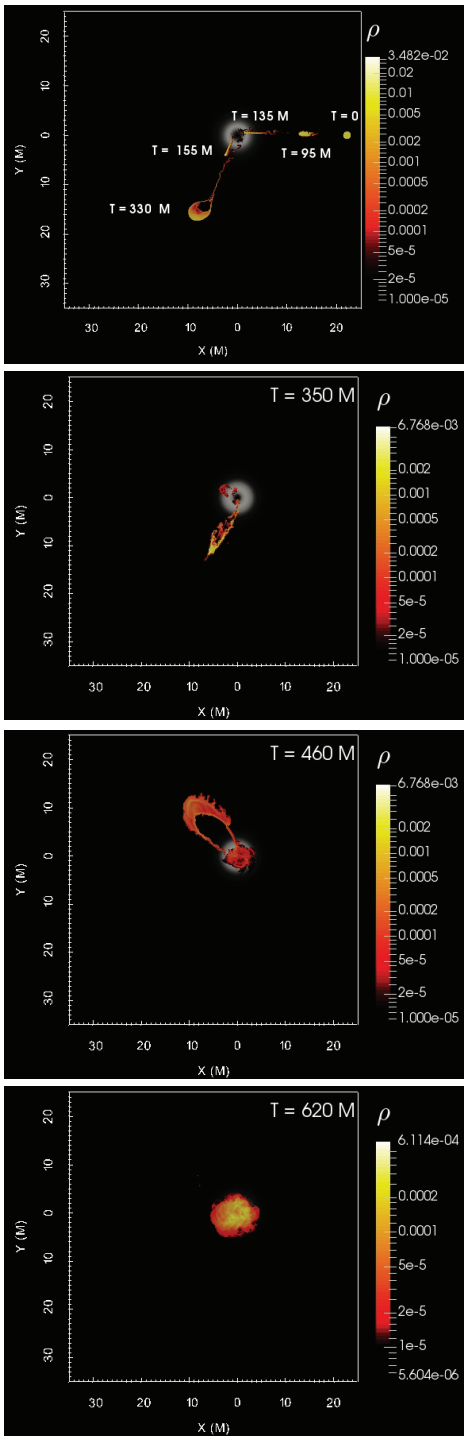


**Figure 4.** Case A. Colormaps of the density (in units of $n_0 M$) of the cloud in the vicinity of a typical boson torus during the various phases of free-fall experienced by the cloud.

effect. The resulting shape of the cloud is a drop-shape cloud with large radial expansion while its tail is expanding down to the BS center (figure 4). Such disruption of the cloud leads to a drop in density and thermal pressure (figure 1).

*4.1.4. Falling back onto the BS.* Once the cloud has reached a distance of $r = 40\,M$ from the BS at time $T \approx 330M$ the cloud undergoes a sudden deceleration and it is attracted backward onto the BS center (figures 1 and 4). During this phase, the tidal disruption gives rise to a speed stratification within the cloud. Consequently the various parts of the cloud collide, leading to an increase of the density and pressure of the cloud (figure 1).

The tail and head of the cloud reach the center of the BS with different angles because of the differential Lense–Thirring at work in the interior of the BS. When the cloud emerges once again from the other side of the BS, each part of the cloud follows different geodesic and once more a drop-shape form appears on the other side (figure 4). However, the drop-shape has a larger extension and when it reaches a distance $r = 10\,M$ from the center, the cloud is attracted once again toward the BS. Multiple internal collisions between various parts of the cloud occur leading to a local enhancement of the cloud pressure an breaks the flow toward the center of the BS. The gas initially contained in the cloud then starts to move on circular orbits near the BS center and no gas is leaving the object.

During this last phase and after successive shocks, three vortex appear in the gas. A large vortex is visible in the center of the BS while two smaller ones are rotating in opposite direction. The center of the larger vortex coincides with the geometrical center of BS. The two smaller ones are rotating in opposite direction along the maximum BS scalar field. The formation of the disk occurs originally from a ring of cloud gas whose radius corresponds to the last stable orbit, namely inside the boson torus (i.e. the maximum of the scalar field). Eventually, the gas is diffused through all circular orbits in the BS which leads to a differentially rotating disk.

### *4.2. Close cloud around a typical boson star ($k = 1$ and $\omega = 0.8\ m/\hbar$)—Case B*

The first simulation was dealing with a cloud experiencing a free-fall onto a BS from a rather large distance, hence considering a cloud whose approaching velocity is large. In order to assess the dynamics of a slower falling cloud, we choose to reenact the simulation with a cloud initially closer to the BS and a vanishing initial velocity. Our second simulation (Case B) stands for a simulation considering the exact same model of BS than the previous case while setting the initial position of the cloud at a much shorter distance from the center of the BS, namely $r_{\rm init} = 3\,M$. Such position lies in the vicinity of the maximum of the scalar field ($r_{\rm boson} = 2.8\,M$). The position of the center of the cloud actually coincides with the maximum of the radial derivative of the lapse function thus locally the radial tidal force is strong (figure 3). Let us note that toward the center of the BS, the radial gravitational force decreases rapidly and even changes sign leading to a radially repulsive force within the inner region as discussed in Meliani *et al* (2016). Within this inner region, the toroidal frame dragging which is null at the center of the BS, reaches its maximum $\beta^{\varphi} = 0.125\,c$ near the initial position of the cloud (figure 3). Such initial setup leads to a prevailing Lense–Thirring effect compared to the local tidal forces.

In the initial phase of the simulation, the cloud accelerates toward the center under the influence of the gravitation field. Acceleration is taking place with a dominant toroidal component induced by the Lense–Thirring effect which leads to a speed of $v \sim 0.1\,c$. During this phase the cloud undergoes a weak transverse compression. As the cloud reaches the region of

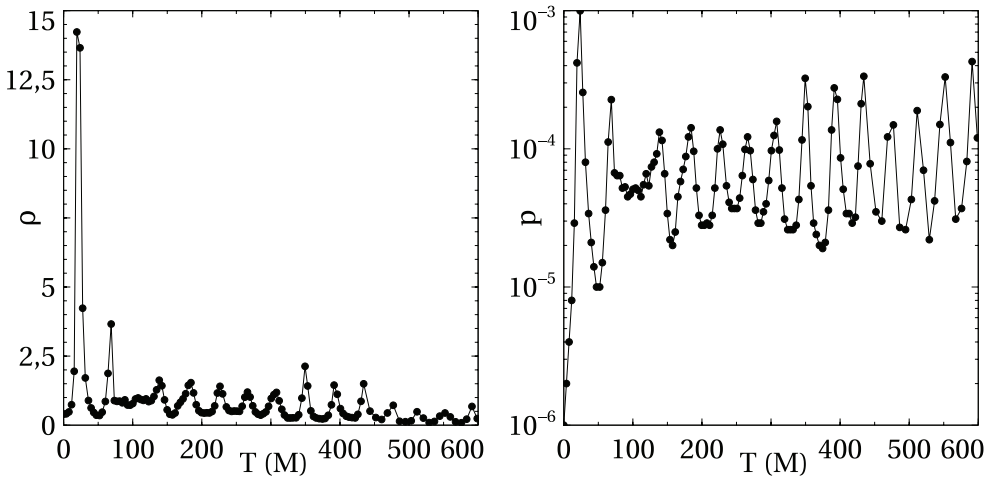


**Figure 5.** Case B. Left: temporal evolution of the maximum density $\rho$(in units of $n_0 M$) of the cloud. Right: temporal evolution of the maximum pressure $p$(in units of $n_0 M c^2$) of the small cloud oscillating in the inner region of boson torus with $k = 1$ and $\omega = 0.8\ m/\hbar$.

maximal scalar field, it is accelerated radially toward the center. It then experiences a strong transverse compression where its pressure rises to a thousand time the initial pressure (figure 5, right). However the cloud keeps its drop-shape (figure 7) since the characteristic compression time remains larger than the cloud propagation time within the inner region of the BS.

When the cloud crosses the BS center, it deviates 60° from its initial course and then propagates outwardly (figure 6). During this phase the transverse gravitational compression decreases enabling the cloud to expand (figure 7). This expansion is anisotropic because of the combined effet of tidal forces and frame dragging. The cloud decompression is then associated with an ejection of gas from the cloud leading to the formation of a tail. The frame dragging has a significant influence upon the outgoing cloud as it induces a strong deviation in its trajectory. Such deviation is possible because of the small radial velocity of the cloud, $v \sim 0.05\,c$. During its outward propagation, the cloud decelerates up to a distance $r_{\max} = 3\,M$. Subsequently it accelerates backward toward the BS once more (figure 6). Inside the region with maximum scalar field, the acceleration occurs mainly toward the center. The Lense–Thirring effect induces a 45° deviation on the cloud orbit in the same direction than the BS rotation near the center of the BS. Throughout this new free fall phase, the cloud goes through a compression process. A pattern can then be identified regarding the motion of the cloud around the BS in case B. This patterns is consistent with a repetitive cycle including a free-falling phase, followed by a significant deviation and by an outwardly orientated motion. Let us note that the precession motion one can identify in figure 6 is always oriented in the same direction than the rotation of the BS.

The compression processes occurring during the first phase is supersonic only near the edges of the cloud. The internal part of the cloud undergoes weaker compressional process. In the final stage of the initial free-fall, the compression of the cloud has become supersonic all over the cloud. A shock wave then propagates toward the center of the cloud with a speed of $v^{\varphi} = 0.06\,c$ and a Mach number of the order of $\mathcal{M} = 3$. The increasing central pressure forces the wave to bounce and to stop the cloud compression. When the cloud crosses the center of the boson torus and moves outward, the high temperature cloud produces a

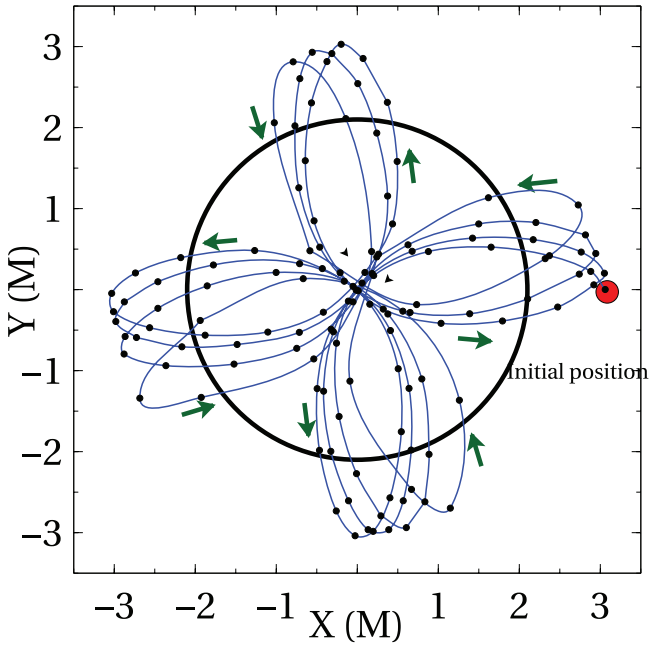


**Figure 6.** Case B. The trajectory of the cloud set a distance of $3M$ from a boson torus with parameter $k = 1$ and $\omega = 0.8\ m/\hbar$. The black circle around the center marks the maximum of the scalar field.

supersonic expansion as the gravitational compression decreases. The cloud reaches its maximum extension at distance $r_{\rm max} = 3\,M$ after which the cloud is moved back to center of the BS. This process repeats itself over each cycle.

During the many cycles of free-falling/escape of the system, the cloud loses a fraction of its mass because of the gravitational compression and following thermal rebound. The gas lost by the cloud first forms a cloud tail. This low speed tail is subject to tidal squeezing and to strong Lense–Tirring. Slowly this cloud tail contributes to low density orbiting disk between the last stable orbit and the maximum of the scalar field.

### *4.3. Remote cloud around a rapidly rotating boson star ($k = 4$ and $\omega = 0.8\ m/\hbar$)—Case C*

This third simulation is consistent with case A where the cloud was initially placed at $r_{\rm start} = 23\,M$ from the BS center but considering a more rapidly rotating model of boson star than in the first simulation. In the beginning of the simulation, the cloud follows the local geodesics with a elongated ellipse-shape (figure 8) as in Grandclément *et al* (2014). The first free-fall motion is mainly performed along the radial direction while the cloud reaches a total velocity of $v \sim 0.7\,c$, close to the escape velocity of this BS. After passing nearby the center, it deviates 60° from its initial course and propagates outwardly until reaching radius $r \sim 21\,M$ from the center. Once reaching this point, it is again attracted backward leading to a trajectory whose form is consistent with a petal-shape. The cloud crosses for the second time the BS center before being attracted for one last time toward the BS. Indeed, after the second crossing of the BS the cloud is attracted one last time and is dislocated to form a disk structure. In the following paragraph, we will describe each phases of the cloud motion and the associated compressional processes.

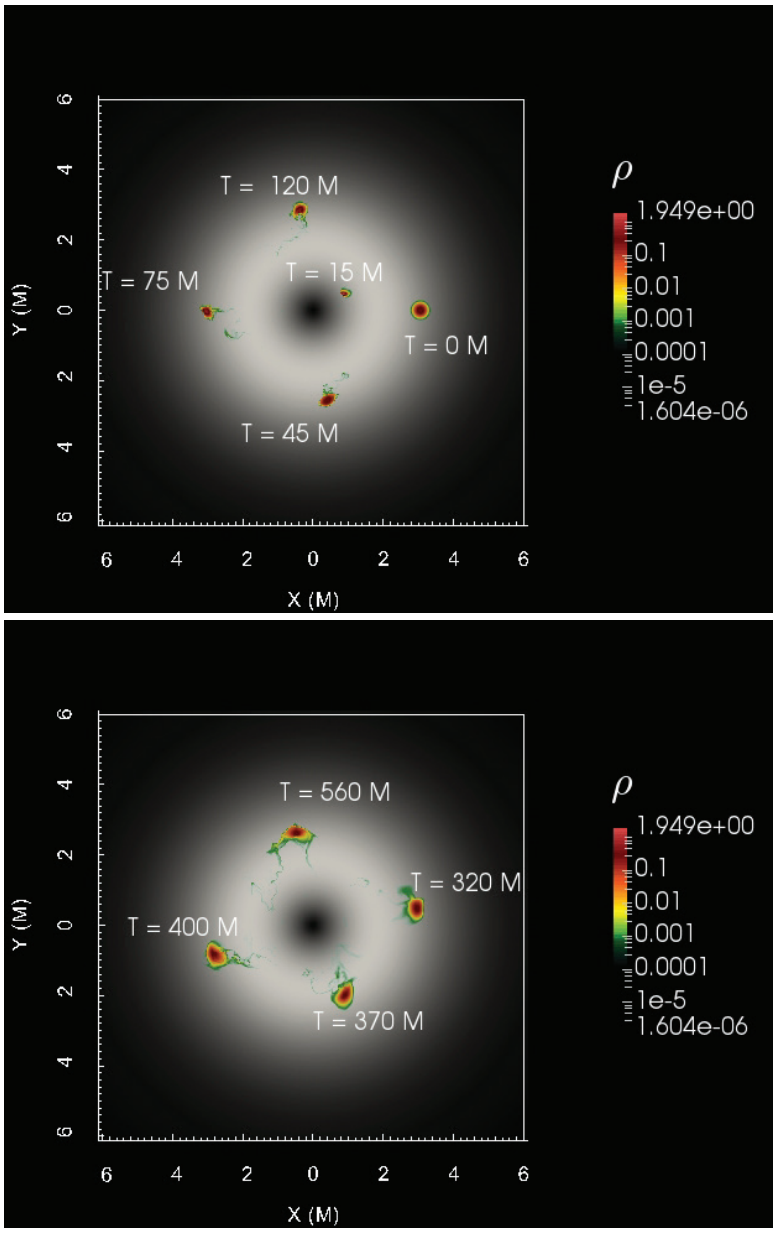


**Figure 7.** Case B. Colormaps of the density (in units of $n_0 M$) of the cloud oscillating in the inner region of boson torus with $k = 1$ and $\omega = 0.8\ m/\hbar$ .

During the first phase, the cloud accelerates toward the center of the BS and undergoes a slow transverse compression supported by successive oblique compressional waves and shock waves propagating from the cloud edge toward the propagation axis (figure 9). The strength of these compressional waves increases as the cloud is closing to the center. Stronger shocks prevail near the edges of the cloud while they get weaker in the center. The results of these compressional and shock waves is a slow increase of the thermal pressure that reaches four times the initial pressure (figure 10). It is noteworthy that around such BS model, the gravity

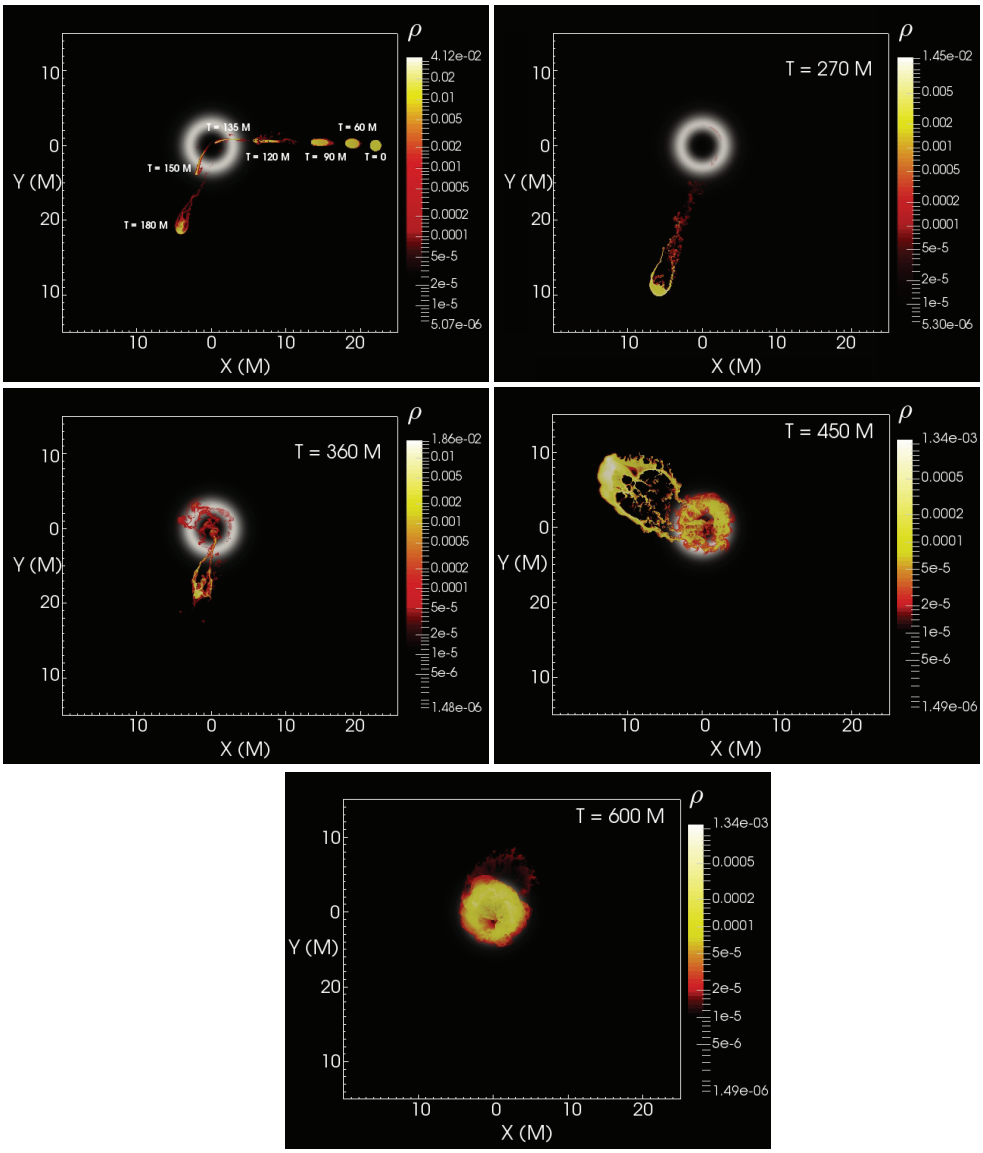


**Figure 8.** Case C. At different time, the density (in units of $n_0\,M$) contour of the cloud free falling phase in the vicinity of boson torus with $k = 4$ and $\omega = 0.8\ m/\hbar$.

of the BS match the ones from a Schwarzschild black hole of equivalent mass at distance larger than $r > 10\,M$ (Meliani *et al* 2016).

Within radius $r < 10\,M$, it can be noticed that the cloud compression increases as thermal pressure reaches 15 times the initial one. At that point a strong shock forms leading to a significant increase of the cloud pressure (figure 10). The resulting structure can be seen at time $T = 135\,M$ in figure 8 (top left) where the cloud is very elongated with a small transverse expansion. As the cloud crosses the BS torus, it deviates toward the geometrical center with a radial speed of $v^{\rm r} \sim 0.7\,c$.

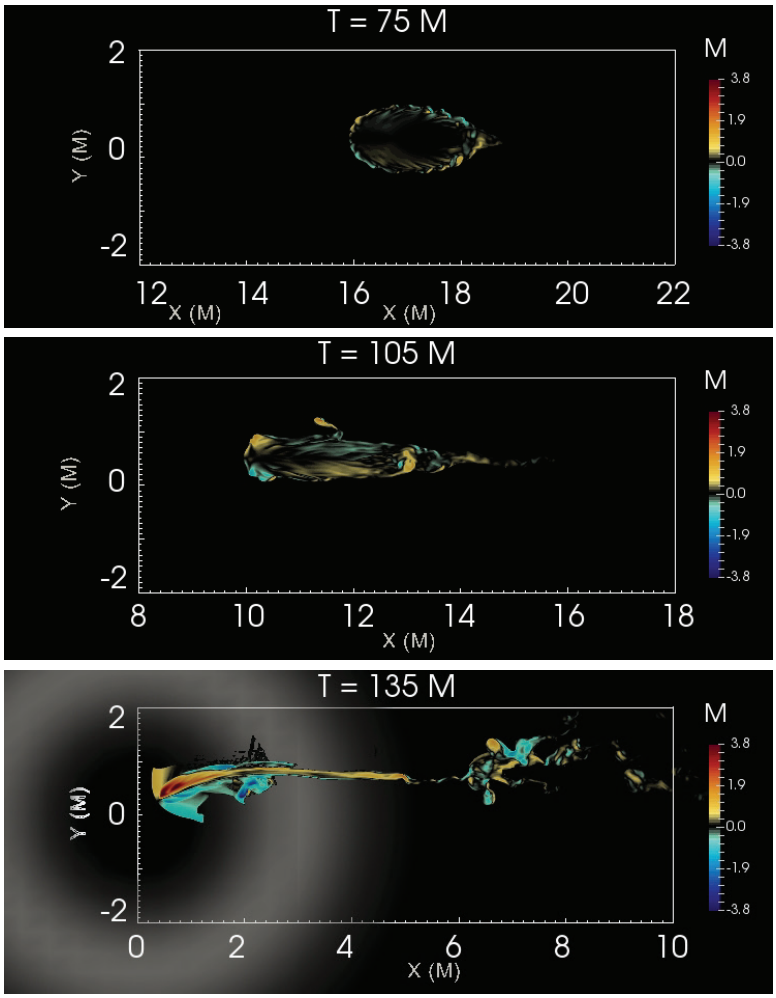


**Figure 9.** Case C. The Mach number in the cloud comoving frame during the first free falling phase in the vicinity of boson torus with $k = 4$ and $\omega = 0.8\ m/\hbar$.

As the cloud escapes outwardly from the center, it moves along a direction having an angle of 60° with respect to the initial free falling direction. The transverse tidal forces then decreases enabling the thermal pressure to produce a transverse expansion of the cloud (figure 8, top-right, $T = 150\,M$). The pressure inside the cloud falls while the cloud propagates far from the BS as a result of the expansion and the elongation of the cloud (figure 8, top-left, $T = 150\,M$ and $T = 180\,M$). After this expansion phase the cloud has a drop-shape with two filaments in the back. The tidal force fragments the cloud moving away. Each fragment propagates with difference speed which gives rise to collisions between them when the head of the cloud starts to decelerate. At time $T = 180\,M$, density increases significantly, whereas pressure is undergoing a smooth increase. Propagating outwardly, the tidal force decreases and the cloud gets a more spherical shape (figure 8) while pressure continues to decrease untill time $T = 270\,M$. Such time corresponds to the most remote position that the cloud can get before falling back onto the BS.

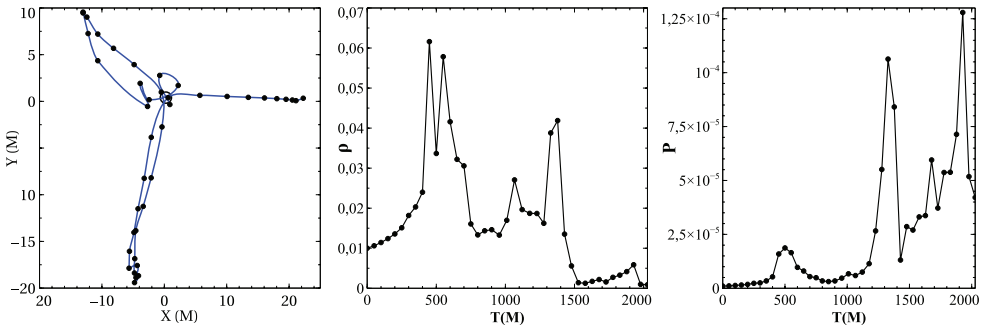


**Figure 10.** Case C. Left: the orbit of the cloud in free falling at the vicinity of boson torus with $k = 4$ and $\omega = 0.8\ m/\hbar$. Center: the maximum density variation. Right: the maximum pressure variation.

Beyond time $T = 270M$, the cloud falls back onto the BS. Initially, the two filaments in the back of the cloud fall first and then collide as they reach the BS center forming a dense highly pressurized stream with low velocity at time $T = 320\,M$ (figure 10). A large fraction of the rest of the cloud falling with a larger speed collides with the aforementioned stream. This collision starts at time $T = 360\,M$ (figure 8) and last until $T = 400\,M$ followed by an increase of the density and pressure (figure 10). The collision between the various part of the cloud induces an ejection of gas onto circular orbits near the center of the BS torus. Let us note that a small fraction of the cloud continues its propagation away from the BS. This gas has a lower speed than the infalling matter and exhibits a complex structure in the radial direction where many shells with different speeds lead to shock formation (Time $T = 450\,M$ in figure 8). After a short propagation distance of about $5\,M$, the escaping gas is falling back onto the BS inducing shocks between the various shells while randomising the energy and momentum hence leading to the deceleration of the cloud in the radial direction. Matter is then distributed to feed the forming disk. In the end, all the gas initially contained inside the cloud starts to orbit within the BS as a turbulent disk. We display a 1D cutof various disk quantities along the radial direction in figure 11. On the three panels, one can see how the radial density and pressure distributions exhibits maximal values near radius $r = 3M$ corresponding to the maximum value of scalar field. The highly unregular shape of this profile suggests that indeed the formed disk is highly turbulent. It is noteworthy that the toroidal speed radial profile shows some vortices structures occurring within the disk, where some regions rotating in same direction than BS and others rotating in counter-direction.

## 5. Discussion

In the previous section we have presented numerical simulations investigating the tidal disruption of gas clouds orbiting around two boson star models. In order to give an overview of such physical process, we ran three different simulations while considering the same cloud but BS model with two different rotation speed. In simulation $(A, C)$, the cloud is set at a large distance from the BS, namely where the spacetime metric matches that of a BH. Both cases $(A, C)$ show the same behaviour where the cloud follows local geodesics with petal-shape orbits (Grandclément *et al* 2014). In both cases, the compressional waves turn into shocks only in the vicinity of the BS center, thus leading to enhanced thermal pressure and density inside the cloud. Shock waves then bounce back in the could and disperse its contains in such

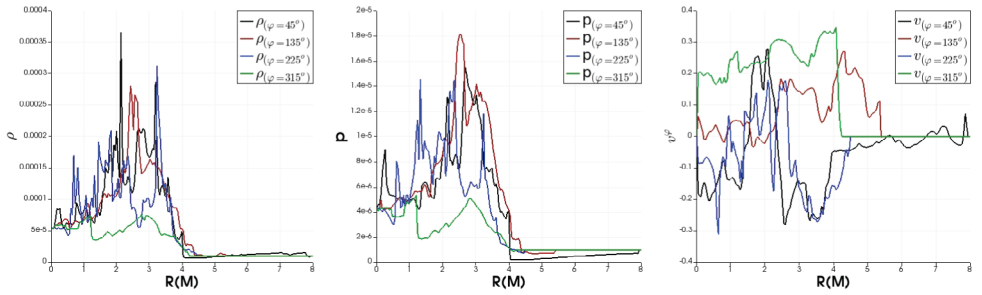


**Figure 11.** Case C. The 1D cut from the geometrical center to radial distance $r \sim 4.5M$ of the density, the pressure and the toroidal component of the speed $v^{\varphi}$ at different angles in the vicinity of boson torus with $k = 4$ and $\omega = 0.8\ m/\hbar$. The black, red, blue, green lines correspond to the cut with respectively angles $\varphi = 45°$, $\varphi = 135°$, $\varphi = 225°$ and $\varphi = 315°$ with $X$-axis.

a way that a disk forms in the inner region of the BS. In these two cases, the cloud passes nearby the center of the BS twice before the gas turns into circularized disks. During this transition phase, the pressure undergoes many flares whose amplitude increases with time until the disk forms (figures 10 and 1). Regarding the density flares, their amplitude decreases with time since a fraction of the gas is ejected from the cloud at each rebound phase. The characteristic time between two flares is constantly decreasing during the temporal evolution. It varies from $\Delta T \sim 150\,M$ to $\Delta T \sim 250\,M$ for the second flare, and then to $\Delta T \sim 100\,M$ for the third flare, and only $\Delta T \sim 60\,M$ for the last one. Such shortening typical flare time interval corresponds to a constant decreases of the distance of the apastron of the cloud orbit. Smaller and smaller distance between the apastron and the BS center is consistent with the cloud losing kinetic energy at each shock-rebound phase (kinetic energy being dissipated into thermal energy).

Simulation $B$ was performed in order to analyse the oscillation of a hot point in the close vicinity of the BS model considered in simulation $A$. Such cloud evolves in a way that is drastically different than around a BH. Among the major differences between the two simulations, the expected compression-rebounds are weaker than in the BH case and requires many passages of the cloud through the BS center before the gas starts to be expelled from the cloud and turns into a disk. It is noteworthy that in this case, the pressure and density flares remain weak compared to a BH case but do have constant time interval $\Delta T \sim 50\,M$. The orbit of a cloud consistent with a 'hot point' remains identical throughout the simulation apart from experiencing a periastron precession induced by the frame-dragging associated with the rotation of the BS.

## 6. Conclusions

In this paper, we have presented the first general relativistic hydrodynamics simulations of gas clouds subject to tidal disruption induced by boson stars. Considering two types of boson stars, we investigated the effects of the initial position of the cloud on both its free-fall trajectory and its compression by tidal forces generated by the boson star. We performed our computations using the GRHD code GR-AMRVAC in Cartesian quasi-isotropic coordinates. Setting a spherical gas at rest in the vicinity of a boson star, we followed its propagation and monitored the temporal evolution of its main features such as the general shape of the gas as well as its internal density and pressure variations. One of the main results from our simulations is that

the trajectory of the cloud is very dependent on its initial position. Indeed when the cloud is initially set in the close vicinity a BS, the resulting trajectory is initially an elliptic orbit. On the other hand, clouds falling from larger distance from the BS travel along orbits that a:re more elongated and do have petal-shape as in Grandclément *et al* (2014). In such cases the cloud mainly follows the local geodesic except when the internal pressure is building up with shocks occurring. At such moment, the trajectory of the cloud experiences deviations from the local geodesic, hence modifying the propagation of the cloud. As the cloud is propagating from the interior of the BS to the outer star region, it is subject to successive shock waves resulting from the tidal compression and thermal rebound. When the cloud comes close enough to a compact objects such as a boson stars, strong gravitational forces act on the cloud in such a way that a large amount of gas is teared off from the cloud. In some cases, the cloud can even be completely torn apart by the tidal forces. Matter ejected from the cloud is captured between the last stable orbit and the center of boson torus. We show that if the cloud falls from large distance, there will be a limited number of pressure and density flares exhibiting a decreasing intensity with time. Regarding the dynamics of a hot point (cloud set at short distance), flares occurs permanently in both pressure and density with constant time interval given mainly by the initial the position of the hot point.

## Acknowledgments

Part of this work was supported by the PNHE. This work acknowledges financial support from the UnivEarthS Labex program at Sorbonne Paris Cité (ANR-10-LABX-0023 and ANR-11-IDEX-0005-02). All the the computations made use of the High Performance Computing OCCIGEN and JADE at CINES within the DARI project c2015046842. Part of this work was supported by the Observatoire de Paris.

## ORCID iDs

Z Meliani https://orcid.org/0000-0002-7495-3897

## References

Anninos P, Fragile P C, Wilson J and Murray S D 2012 Three-dimensional moving-mesh simulations of galactic center cloud G2 *Astrophys. J.* **759** 132

Baganoff F K *et al* 2001 Rapid x-ray flaring from the direction of the supermassive black hole at the galactic centre *Nature* **413** 45–8

Bloom J S *et al* 2011 A possible relativistic jetted outburst from a massive black hole fed by a tidally disrupted star *Science* **333** 203

Bonazzola S and Pacini F 1966 Equilibrium of a large assembly of particles in general relativity *Phys. Rev.* **148** 1269–70

Brassart M and Luminet J P 2010 Relativistic tidal compressions of a star by a massive black hole *Astron. Astrophys.* **511** A80

Burrows D N *et al* 2011 Relativistic jet activity from the tidal disruption of a star by a massive black hole *Nature* **476** 421–4

Carter B and Luminet J P 1982 Pancake detonation of stars by black holes in galactic nuclei *Nature* **296** 211–4

Cenko S B *et al* Swift j2058.4+0516: discovery of a possible second relativistic tidal disruption flare? *Astrophys. J.* **753** 77

Donnarumma I and Rossi E M 2015 Radio-x-ray synergy to discover and study jetted tidal disruption events *Astrophys. J.* **803** 36
Fishbone L G 1973 The relativistic roche problem I. Equilibrium theory for a body in equatorial, circular orbit around a Kerr black hole *Astrophys. J.* **185** 43–68
Frank J and Rees M J 1976 Effects of massive central black holes on dense stellar systems *Mon. Not. R. Astron. Soc.* **176** 633–47
Gezari S *et al* 2006 Ultraviolet detection of the tidal disruption of a star by a supermassive black hole *Astrophys. J.* **653** L25–8
Grandclément P, Somé C and Gourgoulhon E 2014 Models of rotating boson stars and geodesics around them: new type of orbits *Phys. Rev.* D **90** 024068
Grould M, Meliani Z, Vincent F, Grandclément P and Gourgoulhon E 2017 Comparing timelike geodesics around a Kerr black hole and a boson star *Phys. Rev.* D
Guzmán F S and Rueda-Becerril J M 2009 Spherical boson stars as black hole mimickers *Phys. Rev.* D **80** 084023
Harten A, Lax P D and van Leer B 1983 *SIAM Rev.* **25** 35
Hayasaki K, Stone N and Loeb A 2013 Finite, intense accretion bursts from tidal disruption of stars on bound orbits *Mon. Not. R. Astron. Soc.* **434** 909–24
Hills J G 1975 Possible power source of Seyfert galaxies and QSOs *Nature* **254** 295–8
Kaup D J 1968 Klein–Gordon Geon *Phys. Rev.* **172** 1331–42
Kobayashi S, Laguna P, Phinney E S and Mészáros P 2004 Gravitational waves and x-ray signals from stellar disruption by a massive black hole *Astrophys. J.* **615** 855–65
Komossa S and Greiner J 1999 Discovery of a giant and luminous x-ray outburst from the optically inactive galaxy pair RX J1242.6-1119 *Astron. Astrophys.* **349** L45–8
Komossa S, Halpern J, Schartel N, Hasinger G, Santos-Lleo M and Predehl P 2004 A huge drop in the x-ray luminosity of the nonactive galaxy RX J1242.6-1119A, and the first postflare spectrum: testing the tidal disruption scenario *Astrophys. J.* **603** L17–20
Koren B and van der Maarel H T M 1993 Monotone, higher-order accurate, multi-dimensional upwinding *Numerical Methods in Fluid Dynamics* (*Lecture Notes in Physics* vol 414) ed M Napolitano and F Sabetta (Berlin: Springer) pp 110–4
Liebling S L and Palenzuela C 2012 Dynamical boson stars *Living Rev. Relativ.* **15** 6
Luminet J P and Marck J A 1985 Tidal squeezing of stars by Schwarzschild black holes *Mon. Not. R. Astron. Soc.* **212** 57–75
Marck J A, Lioure A and Bonazzola S 1996 Numerical study of the tidal interaction of a star and a massive black hole *Astron. Astrophys.* **306** 666
Meliani Z, Grandclément P, Casse F, Vincent F H, Straub O and Dauvergne F 2016 GR-AMRVAC code applications: accretion onto compact objects, boson stars versus black holes *Class. Quantum Grav.* **33** 155010
Meliani Z, Vincent F H, Grandclément P, Gourgoulhon E, Monceau-Baroux R and Straub O 2015 Circular geodesics and thick tori around rotating boson stars *Class. Quantum Grav.* **32** 235022
Metzger B D, Giannios D and Mimica P 2012 Afterglow model for the radio emission from the jetted tidal disruption candidate swift J1644+57 *Mon. Not. R. Astron. Soc.* **420** 3528–37
Nikołajuk M and Walter R 2013 Tidal disruption of a super-jupiter by a massive black hole *Astron. Astrophys.* **552** A75
Nolthenius R A and Katz J I 1983 The infall of a star into a massive black hole *Astrophys. J.* **269** 297–302
Piran T, Sądowski A and Tchekhovskoy A 2015 Jet and disc luminosities in tidal disruption events *Mon. Not. R. Astron. Soc.* **453** 157–65
Rosswog S, Ramirez-Ruiz E and Hix W R 2009 Tidal disruption and ignition of white dwarfs by moderately massive black holes *Astrophys. J.* **695** 404–19
Ruffini R and Bonazzola S 1969 Systems of self-gravitating particles in general relativity and the concept of an equation of state *Phys. Rev.* **187** 1767–83
Saxton R D, Motta S E, Komossa S and Read A M 2015 Was the soft x-ray flare in NGC 3599 due to an AGN disc instability or a delayed tidal disruption event? *Mon. Not. R. Astron. Soc.* **454** 2798–803
Schartmann M, Burkert A, Alig C, Gillessen S, Genzel R, Eisenhauer F and Fritz T K 2012 Simulations of the origin and fate of the galactic center cloud G2 *Astrophys. J.* **755** 155
Schunck F E and Mielke E W 2008 Topical review: general relativistic boson stars (arXiv:0801.0307)
Servillat M, Farrell S A, Lin D, Godet O, Barret D and Webb N A 2011 X-Ray variability and hardness of ESO 243-49 HLX-1: clear evidence for spectral state transitions *Astrophys. J.* **743** 6

Shiokawa H, Krolik J H, Cheng R M, Piran T and Noble S C 2015 General relativistic hydrodynamic simulation of accretion flow from a stellar tidal disruption *Astrophys. J.* **804** 85

Stone N, Sari R and Loeb A 2013 Consequences of strong compression in tidal disruption events *Mon. Not. R. Astron. Soc.* **435** 1809–24

van Velzen S, Farrar G R, Gezari S, Morrell N, Zaritsky D, Östman L, Smith M, Gelfand J and Drake A J 2011 Optical discovery of probable stellar tidal disruption flares *Astrophys. J.* **741** 73

Vincent F H, Meliani Z, Grandclément P, Gourgoulhon E and Straub O 2016 Imaging a boson star at the galactic center *Class. Quantum Grav.* **33** 105015

Vinkó J, Yuan F, Quimby R M, Wheeler J C, Ramirez-Ruiz E, Guillochon J, Chatzopoulos E, Marion G H and Akerlof C 2015 A luminous, fast rising UV-transient discovered by ROTSE: a tidal disruption event? *Astrophys. J.* **798** 12

Wheeler J A 1955 Geons *Phys. Rev.* **97** 511–36

Zhao H, Haehnelt M G and Rees M J 2002 Feeding black holes at galactic centres by capture from isothermal cusps *New Astron.* **7** 385–94